Self-compression by femtosecond pulse filamentation: Experiments versus numerical simulations

Stefan Skupin,[1,*] Gero Stibenz,[2] Luc Bergé,[1] Falk Lederer,[3] Thomas Sokollik,[2] Matthias Schnürer,[2] Nickolai Zhavoronkov,[2] and Günter Steinmeyer[2]

[1]*Département de Physique Théorique et Appliquée, CEA-DAM/Ile de France, B.P. 12, 91680 Bruyères-le-Châtel, France*

[2]*Max-Born-Institut für Nichtlineare Optik und Kurzzeitspektroskopie, Max-Born-Straße 2a, 12489 Berlin, Germany*

[3]*Institute for Condensed Matter Theory and Solid State Optics, Friedrich-Schiller-Universität Jena, Max-Wien-Platz 1, 07743 Jena, Germany*

(Received 11 July 2006; published 6 November 2006)

We analyze pulse self-compression in femtosecond filaments, both experimentally and numerically. We experimentally demonstrate the compression of 45 fs pulses down to a duration of 7.4 fs at millijoule pulse energies. This sixfold compression in a self-generated filament does not require any means for dispersion compensation and is highly efficient. We compare our results to numerical simulations, providing a complete propagation model that accounts for full dispersion, pressure variations, Kerr nonlinearity and plasma generation in multiphoton and tunnel regimes. The equations are numerically integrated and allow for a quantitative comparison with the experiment. Our experiments and numerical simulations reveal a characteristic spectrotemporal structure of the self-compressed pulses, consisting of a compressible blue wing and an incompressible red pedestal. We explain the underlying mechanism that leads to this structure and examine the scalability of filament self-compression with respect to pulse energy and gas pressure.

DOI: 10.1103/PhysRevE.74.056604 PACS number(s): 42.65.Tg, 52.38.Hb, 42.68.Ay

I. INTRODUCTION

Combining linear and nonlinear pulse shaping mechanisms for the compression of laser pulses [1] to ever shorter durations is a proven concept in femtosecond laser physics, enabling the generation of pulses with durations approaching the optical cycle [2]. Self-phase modulation, commonly used as the nonlinear ingredient of pulse compression schemes, generates new spectral content in the wings of the pulse. Carefully adjusted dispersion, acting as the linear counterpart, pulls the newly generated spectral components back into the temporal center of the pulse. The exact balance of these two processes can give rise to stable pulse shapes known as optical solitons [3,4], which, in the absence of dissipation, can propagate indefinitely in optical fibers without changing their shape. Moreover, higher-order solitons can also be exploited for pulse shortening [5], without necessity for external dispersion compensation.

The concept of temporal solitons was readily extended to the spatial domain [6], with self-trapped beam profiles arising from the competition of diffraction and self-focusing. Such beams propagate without being diffracted for extended lengths in a nonlinear medium. Using intense femtosecond laser pulses, similar self-trapping was also observed for the competition of Kerr-type self-focusing and the defocusing action of free electrons generated via photoionization of the ambient atoms. This process is also referred to as filamentation [7]. Ultrashort pulses with powers above the critical power for self-focusing produce a narrow self-generated waveguide with a length substantially exceeding the Rayleigh length of the beam. Ultimately, it is desirable to combine both, spatial self-channeling and temporal compression, for the formation of an "optical light bullet" [8], i.e., aspatiotemporal wave packet that contracts itself as close as possible to the optical cycle in either dimension, with the self-contraction being accompanied by an intensity increase of several orders of magnitude. The temporal evolution of femtosecond pulses during filament formation has been shown to exhibit self-compression, both theoretically [9–13] and also experimentally [14–16]. In the turn of filamentary beam stabilization, an ionization front is generated that will also affect the subsequent temporal structure of the pulse via plasma defocusing and cause damping of the trailing part of the pulse. This single-sided depletion can give rise to some effective pulse compression [10]. However, other effects such as chromatic dispersion, pulse steepening, and nonlinear losses limit this shortening mechanism. The rear pulse may eventually refocus, which usually produces a characteristic double-peaked temporal distribution [17,18], with either peak occupying a temporal extension of the order of the input pulse duration. Proper pulse compression to the few-cycle regime, instead, requires the isolation of one (at least dominant) peak shortened relative to the input pulse.

Exploitation of combined spatial and temporal shaping for efficient compression of an isolated femtosecond pulse has been subject to extensive experimental [14–16,19] and theoretical investigations, both in gaseous media [10–12,17,18] as well as in solid dielectrics [9,20–22]. For example, it was numerically demonstrated that plasma-induced subpulses with duration down to a single optical cycle can propagate for tens of centimeters in pressurized argon cells [11]. Later, Hauri *et al.* used a configuration of two cascaded gas-filled cells with intermittent and subsequent dispersion compensation for producing submillijoule light pulses with durations down to 5.7 fs [19]. It was later suggested that this scheme could be further improved when a single cell with a pressure gradient is used instead, potentially resulting in pulses with a single-cycle temporal signature [12]. Despite some first results with pressure gradients that were mainly directed at compression with higher pulse energies [23], it appears

*Electronic address: stefan.skupin@cea.fr

cumbersome to adjust the pressure gradient for optimum compression to extremely short pulse duration. In a recent experimental demonstration, Stibenz *et al.* demonstrated highly efficient pure self-compression of 45 fs pulses down to below 10 fs duration, obliterating the need for any kind of dispersion compensation, pressure gradients, or capillaries for beam guiding [16]. The physical mechanism enabling this simple self-compression scheme for generation of sub-10-fs pulses with several millijoule of pulse energy, however, is still not fully understood.

In this work, we will conduct a careful analysis of our experimental data on self-compression in femtosecond filaments and compare these to an extensive numerical model. For the first time we demonstrate *quantitative agreement* between the self-compression experiments and the numerical model. This agreement is pushed to the point that numerical simulations do reproduce filament range, temporal distributions, together with the intensity and phase spectra as those achieved in the laboratory. Our numerical simulations indicate a small parameter range, in which a delicate balance between beam power, input waist, and focusing geometry prevents secondary or oscillatory refocusing events in the evolution of the filament. Once collapsed, the beam propagates in a stable beam geometry for up to 50 cm. This is also confirmed in our experiments. Inside the gas cell, we observe isolated fluorescence channels stretching over up to 50 cm length, indicative of plasma channel and beam confinement in this region. Simultaneously, the blue wing of the pulse is compressed in the temporal domain down to about 10 fs pulse duration, with an excellent agreement between numerical model and experimental results.

The paper is organized as follows: in Sec. II we will provide a detailed analysis of our experimental results on self-compression in argon and krypton, revealing a characteristic structure of the pulses generated in the filament. Our experimental account will be complemented by corresponding numerical results in Sec. III. Detailed insight into the propagation dynamics allows us to explain the pulse shortening mechanism. Furthermore, we analyze the influence of various input parameters such as beam waist, energy, gas pressure, and focusing geometry on the propagation dynamics. We will subsequently discuss and compare experimental and theoretical findings (Sec. IV) and end with an outlook on the further potential of the method described.

II. EXPERIMENT

For our experimental investigations on self-compression in femtosecond filaments, we employed two different laser sources. Most experiments were carried out with a Ti:sapphire amplifier system that delivers 45 fs pulses at a repetition rate of 1 kHz, a center wavelength of 803 nm, and up to 5 mJ pulse energy [24]. This laser system consists of a first-stage regenerative amplifier, delivering 1.7 mJ of pulse energy, and a subsequent dual-pass booster amplifier, employing a cooled Ti:sapphire crystal ($T=213$ K). Compared to other Ti:sapphire laser systems with comparable energy, this laser exhibits an extremely clean beam profile (Strehl ratio ≈ 0.97, corresponding to an rms wave-front distortion of

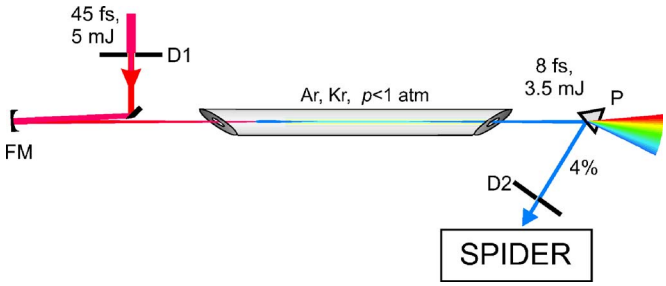

FIG. 1. (Color online) Setup employed in the experiments. FM, focusing mirror; D1, D2, adjustable diaphragms; P, prism used for beam attenuation; SPIDER, pulse characterization system.

1/40 wave) and very small pulse-to-pulse energy fluctuations of 0.3% (rms). Further experiments were carried out with a 10 Hz Ti:sapphire amplifier system, capable of delivering pulses with up to 100 mJ energy at 40 fs FWHM duration.

The laser output is focused into a gas cell with dielectric concave mirrors as shown in Fig. 1. The cell is filled with a noble gas, the pressure being adjustable between zero and atmospheric pressure. The cell is equipped with two Brewster-angled silica windows. For the experiments with the kHz laser, we used 1 in. diameter windows of 0.5 mm thickness and a cell length of 1 m. For focusing an $f=1.5$ m mirror was employed. The high-energy experiments were carried out with 2 in. diameter windows of 1 mm thickness, an $f=2.5$ m mirror, and the cell was expanded to 3 m length. We found it useful to insert a diaphragm between laser and focusing mirror to adjust power levels to just below the onset of multifilamentation inside the gas cell. The output of the cell is diagnosed by a spectrograph and by spectral phase interferometry for direct electric-field reconstruction (SPIDER [25–27]). To avoid damage in the nonlinear crystal of the pulse characterization setup, the beam had to be attenuated by about a factor 100. This was done in two steps, first by reflecting the beam off the first surface of a silica wedge (prism) and then further by inserting an adjustable diaphragm into the beam. The silica prism was placed such that the beam had already widened substantially to avoid surface damage or any nonlinear effects in the attenuation process. The diaphragm D2 was set to transmit the central part of the beam, corresponding to 10% to 20% of the pulse energy. The experimental results shown therefore reflect the central part of the beam profile, but not an average over the total beam diameter. It must be emphasized that we did not introduce negative dispersion in between gas cell and diagnostics, which sets our experiments apart from earlier approaches to filament compression [19].

Filament compression requires a careful tuning of the nonlinear dynamics inside the gas cell. When power levels are chosen too low, the limited spectral broadening allows only for marginal compression of the pulse duration. On the other hand, multifilamentation sets in if pressures or power levels are chosen too high. Therefore optimum performance is to be expected right below the onset of the beam breakup. Using argon and input energies of 2.5 mJ, multifilamentation sets in slightly above 60 kPa; filaments in krypton stay stable up to 30 kPa. The dispersion of the output window and the

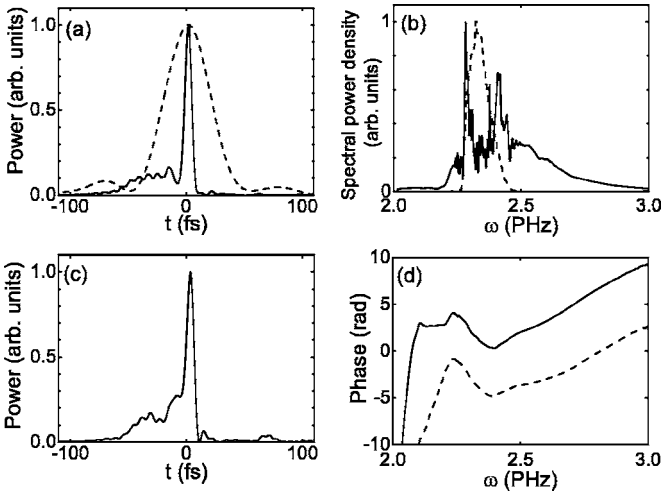

FIG. 2. Characterization of self-compressed pulses generated in a 30 kPa krypton atmosphere. Input energy, 2.5 mJ; output energy, 2 mJ. (a) Output pulse shape of a 7.4 fs pulse (solid line) in comparison to the 45 fs input pulse (dashed line). Pulse shapes are normalized to equal peak power. (b) Corresponding spectra normalized to equal peak power density. (c) Output pulse with 7.8 fs duration. (d) Spectral phases recorded by SPIDER. The solid line corresponds to the transient displayed in (a), the dashed line to the one in (c).

air path to the SPIDER setup amount to 80 fs^2 for the low-energy kHz system, and to 160 fs^2 for the high-energy experiments. Therefore, measurement of pulses with a flat spectral phase imply generation of slightly negatively chirped pulses within the filament. In fact, we even found it necessary to introduce additional positive dispersion between filament cell and diagnostics in some of the experiments described in Ref. [16].

Figure 2 shows several results obtained in the critical regime in krypton at a pressure of 30 kPa. A typical pulse shape as observed at the output of the cell is depicted as the solid line in Fig. 2(a). This particular pulse has a FWHM duration of 7.4 fs. For comparison, the 45 fs input pulse shape is also shown as a dashed line, clearly revealing a sixfold decrease in pulse duration as a consequence of the self-compression in the filament. Corresponding spectra are shown in Fig. 2(b). The pulse shapes are quite characteristic, as shown by a second independent measurement with 7.8 fs duration [Fig. 2(c)]. This pulse shows a similar asymmetric pulse shape, consisting of one isolated peak and a leading pedestal structure with a duration of about 50 fs. It should be pointed out that experimental parameters have been optimized to generate the shortest pulses in the diagnostic system, which incorporates dispersion of the output window and the air path to the diagnostics. However, the transients in Figs. 2(a) and 2(c) are modified by this small dispersion, leading to a change in pulse duration of a few femtoseconds only, yet still much shorter than the input pulse. Therefore the observed short pulses are a manifestation of self-compression by the filamentation process and only minimally affected by the dispersion in the beam path.

The nonlinear dynamics of the filament also has a characteristic fingerprint in the spectral domain with much stronger

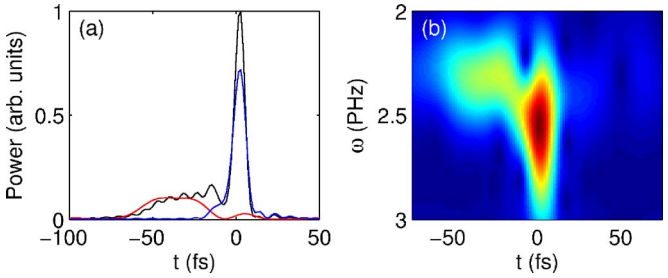

FIG. 3. (Color online) Analysis of the self-compression mechanism. (a) Pulse shape from Fig. 2(a) (solid line) in comparison to the temporal shape of the blue and red part of the spectrum (blue and red lines, respectively), separated at $\omega=2.4$ PHz. The energy content in the pedestal is 40% of the detected pulse energy. (b) Calculated XFROG trace of the pulse shown in (a), assuming an unchirped 10 fs (FWHM) Gaussian reference pulse.

spectral broadening on the blue side than on the red side of the spectrum. While the blue shoulder of the broadened spectrum is rather smooth, the vicinity of the pump wavelength is dominated by several spectrally isolated spikes. Some spectrally narrow features appear to be generated in the cell windows. For the most part, however, these spikes originate from the filamentation process taking place inside the cell. Figure 2(d) shows measured spectral phases corresponding to the two compressed pulses displayed in Figs. 2(a) and 2(c). Quite characteristically, these spectral phases display a recurring kink located at the blue edge of the pump spectrum at $\omega \approx 2.4$ PHz. It is well known that the SPIDER technique may produce a similarly looking phase kink artifact [26,28]. To exclude such an artifact we made careful checks to ensure the integrity of the SPIDER data at the location of the kink. As will be discussed below, the occurrence of similar spectral kinks in the numerical data (cf. Fig. 6) further supports us in excluding such an artifact. The slope discontinuity corresponds to a difference in group delay between adjacent segments, i.e., our spectra essentially decompose into two parts that have been separated in group delay inside the filament. The red part covers the spectral range of the pump pulse, whereas the blue part extends over the newly generated spectral content in the short wavelength wing of the spectrum. Based on the data in Figs. 2(a) and 2(c), this is further analyzed in Fig. 3(a), which displays the pulse shapes reconstructed from the blue part of the spectrum only ($\omega > 2.4$ PHz), as compared to the one resulting from the red part only. Clearly, the latter gives rise to a leading uncompressed pedestal structure whereas self-compression appears to be limited to the blue part of the spectrum, giving rise to the trailing isolated sub-10-fs structure observed in Fig. 2.

An alternative way of visualizing the spectrotemporal structure of the self-compressed pulses is shown in Fig. 3(b). Assuming an unchirped 10-fs Gaussian reference pulse, we computed cross-correlation frequency-resolved optical gating (XFROG) traces [29] from the measured experimental data. Note that this choice of a short reference pulse provides high temporal but low spectral resolution. XFROG traces allow for an intuitive interpretation of the spectrotemporal structure of a pulse [30]. For our experimental situation, the XFROG analysis clearly identifies a self-compressed blue

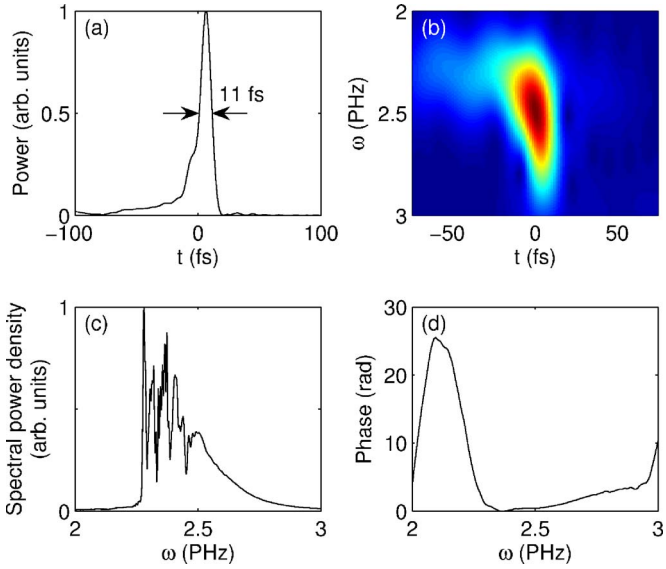

FIG. 4. (Color online) Characterization of self-compressed pulses generated in a 50 kPa argon atmosphere. Input energy, 4.5 mJ; output energy, 3 mJ. (a) Temporal pulse shape as measured. The energy content of the pedestal is 20% of the detected pulse energy. (b) XFROG trace assuming an unchirped 10 fs (FWHM) Gaussian reference pulse. (c) Spectral power density. (d) Spectral phase, with the group delay adjusted for optimal visibility.

section of the pulse at zero delay, centered at $\omega=2.5$ PHz and a separated pedestal pulse located at a delay of ≈ -15 fs and at $\omega=2.2$ PHz. The shape of the XFROG spectrogram is very characteristic, resembling the mirror image of the greek letter Γ. This Γ shape will reappear in the subsequent discussion, however, with varying temporal separation and weight between the two sections. In the XFROG representation dispersive effects can be easily accounted for as they chiefly induce a horizontal shear of the traces shown. Therefore it will be possible to compare experimental and numerical results in Sec. IV, even though some small amount of dispersion from air paths or cell windows may have affected the experimental results.

We further conducted self-compression studies with argon. As argon has a lower nonlinearity, these experiments were performed at a higher pressure compared to krypton to produce the maximum spectral broadening before multifilamentation sets in. The experiments shown in Fig. 4 have been conducted at a pressure of 50 kPa. Figure 4(a) shows the reconstructed temporal profile of a pulse with 11 fs pulse duration. This pulse shows again the characteristic asymmetry of an elongated leading edge and a steep trailing edge. The XFROG analysis in Fig. 4(b) reveals the same Γ structure with a leading red pedestal as seen in the krypton experiments, however, with a less pronounced temporal separation between pedestal and main pulse. Spectral amplitude and phase again show a similar structure as with Kr, with a strongly structured red wing, a smooth blue shoulder, and a phase kink at the transition between the two spectral parts of the pulse.

Using the second laser described in the introduction, we further investigated the scaling behavior of filament compression towards even higher pulse energies. As this laser works at 10 Hz, it exhibits much stronger pulse-to-pulse fluctuations and an inferior beam profile. We could nevertheless confirm self-compression in Ar and Kr also with this laser. For doing so we had to measure over many shots, with only about $\approx 10\%$ of the measurements exhibiting a significant self-compression. This small percentage is due to combined beam-pointing variations and energy fluctuations of the pulses. Self-compression, however, appears to be restricted to a relatively small window of input pulse energies ranging from about 2 to 5 mJ. Even at greatly reduced pressures or using even lighter gases such as neon, we were not able to produce sufficient spectral broadening for 10 fs pulses at higher pulse energies without the onset of multifilamentation.

Our experimental results indicate that compression is most efficient in the newly generated blue wing of the pulse. In general, the red part appears temporally stretched, as already indicated by numerous sharp spectral features in that spectral region. The XFROG reconstructions reveal that the red pedestal is leading, whereas the spectral broadening takes place in the trailing edge of the pulse. As the red pedestal is spectrally separated from the main pulse at least for some of our experimental results, it appears promising to further clean the pulse structure by rejecting the red wing of the spectrum with suitable filters. Moreover, as indicated by the numerical simulations discussed below, the strength of the red pedestal may be affected by distortions in the pulse profile. Shaping of the input pulse or suppression of pulse distortions in the input window may yet hold another possibility to further suppress or reduce this component.

Despite all this insight, any pulse diagnostics is descriptive and restricted to analyzing the output of the filament. With the availability of the spectral phase, one can trace back simple linear effects like dispersion. Yet it is impossible to look directly into the complex nonlinear spatiotemporal pulse shaping processes inside the filament. In the following, we will therefore present numerical simulations of the filamentation in argon and compare it to our experimental findings.

III. SIMULATION

In our numerical simulations we restrict ourselves to propagation in argon for mostly technical reasons. First, more reliable material parameters are available for argon than for krypton. Second, we are quite confident in our implementation of the photoionization for argon, since it was cross-checked against calculations using the time-dependent Schrödinger equation [31,32]. For the moment, we do not have a similar implementation for krypton. Third, our experimental results show that the difference of using argon or krypton in the compressor are of quantitative nature only. Hence, to understand the underlying physics it should be sufficient to study one of the experimental examples.

Let us recall the propagation equations coupling the electric field envelope $\mathcal{E}$ with the electron plasma density ρ (see, e.g., Ref. [33]),

$$\partial_z \mathcal{E} = \frac{i}{2k_0} T^{-1} \nabla_\perp^2 \mathcal{E} + i\mathcal{D}\mathcal{E} + i\frac{\omega_0}{c} n_2 T |\mathcal{E}|^2 \mathcal{E} - i\frac{k_0}{2n_0^2 \rho_c} T^{-1} \rho \mathcal{E} - \frac{\sigma}{2}\rho\mathcal{E} - \frac{U_i W(I)(\rho_{nt} - \rho)}{2I}\mathcal{E}, \quad (1)$$

$$\partial_t \rho = W(I)(\rho_{nt} - \rho) + \frac{\sigma}{U_i}\rho I, \tag{2}$$

where $I=|\mathcal{E}|^2$, $\nabla_\perp^2 = r^{-1}\partial_r r \partial_r$, and $T=1+(i/\omega_0)\partial_t$. The dispersion operator $\mathcal{D}$ is treated in Fourier domain in the form

$$\hat{\mathcal{D}}(\omega) = k(\omega) - k_0 - (\omega - \omega_0) \left.\frac{\partial k}{\partial \omega}\right|_{\omega=\omega_0}, \tag{3}$$

where $k_0 = n_0\omega_0/c = k(\omega_0)$ is the wave number at the laser frequency. Accounting for the pressure dependence of the dispersion relation $k(\omega)$, we re-express it in terms of the linear refractive index n_{at} at atmospheric pressure, i.e.,

$$k(\omega) = \frac{\omega}{c}\sqrt{1 + p[n_{\mathrm{at}}^2(\omega) - 1]}, \tag{4}$$

with p being the pressure ratio with respect to one atmosphere. For argon, the dispersion of n_{at} is given in Ref. [34].

Concerning the value of the nonlinear refractive index n_2 of argon, various values can be found in the literature. References [18,35–37] suggest an index n_2 of about 5×10^{-19} cm^2/W at atmospheric pressure, whereas Refs. [38–41] quote $n_2 \sim 1 \times 10^{-19}$ cm^2/W. Since we observed reasonable quantitative agreement between experiment and simulation with the latter value only, we select $n_2 = 1 \times 10^{-19} p$ cm^2/W throughout this work. However, fine-tuning of this value could be used to further improve the matching between experiment and simulation, but this is beyond our scope and of rather technical interest.

Further on, $\rho_c = 1.73 \times 10^{21}$ cm^{-3} is the critical plasma density at the laser wavelength $\lambda_0 = 800$ nm and $\sigma = 1 \times 10^{-19} p$ cm^2 is the inverse bremsstrahlung cross section [18]. In Eq. (3), $W(I)$ refers to the ionization rate for argon atoms as introduced by Peremolov *et al.* [41]. For the ionization potential we used $U_i = 16$ eV, while $\rho_{nt} = 2.7 \times 10^{19} p$ cm^{-3} is the density of neutral atoms. This model also includes space-time focusing and self-steepening through the operators T, T^{-1}, as established in Ref. [42]. Pulses are assumed to be initially Gaussian,

$$\mathcal{E}(r,t,z=0) = \sqrt{\frac{2P_{\mathrm{in}}}{\pi w_0^2}} \times e^{-r^2/w_0^2 - t^2/t_p^2 - ik_0 r^2/2f}, \tag{5}$$

where P_{in}, w_0, t_p, and f denote input peak power, beam waist, pulse duration, and effective focal length, respectively. Throughout the paper, we will use full-width at half-maximum (FWHM) values with respect to the intensity and beam energy to characterize the input pulses, namely, $t_{\mathrm{FWHM}} = \sqrt{2 \ln 2}\, t_p$, $w_{\mathrm{FWHM}} = \sqrt{2 \ln 2}\, w_0$, and $E_{\mathrm{in}} = \sqrt{\pi/2}\, t_p P_{\mathrm{in}}$.

Simulations assume the entire propagation of the beam in argon at constant pressure. Compared to the actual experimental setup this means the following simplifications: First, we do not take into account that the pulse initially traverses free air instead of argon (1 m). Since this only affects the low-intensity propagation before pulse shortening takes place, it should have small influence on the results. Second, we neglect the propagation through the windows of the argon chamber (0.5 mm), which is justified by their small thickness. Moreover, by doing so we can be sure that the compression really takes place inside the argon cell. Finally, we do not account for the air paths in the experimental diagnostics, but this effect is readily understood in the XFROG diagrams as causing a slight horizontal skew of the XFROG trace.

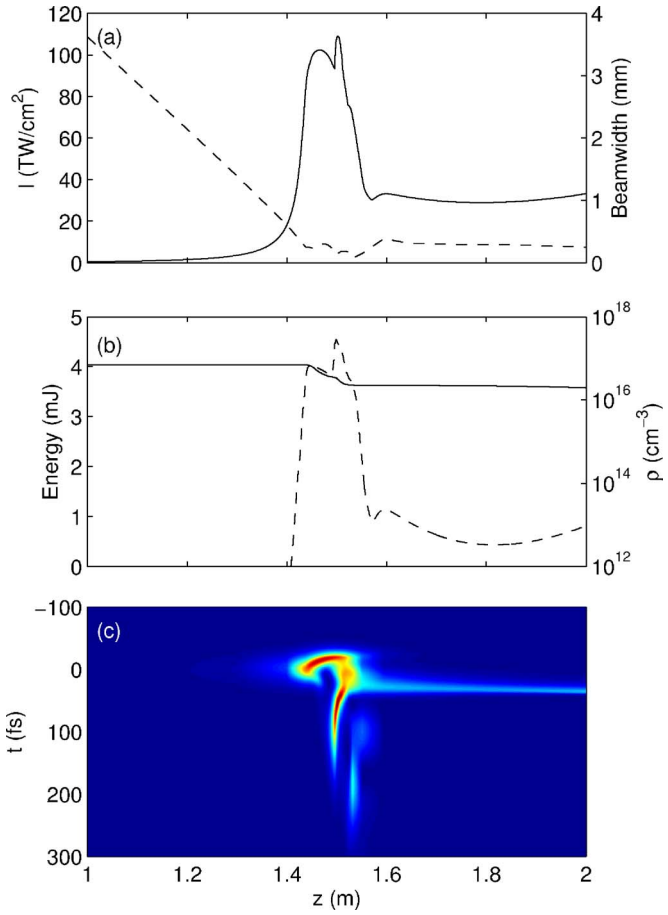

FIG. 5. (Color online) (a) Peak intensity (solid curve) and FWHM of fluence (dashed curve), (b) beam energy (solid curve) and peak electron density (dashed curve) from a 45 fs (FWHM), 11 mm (FWHM), 4 mJ ($P_{\mathrm{in}} = 5P_{\mathrm{cr}}$) initially Gaussian pulse propagating in focused geometry ($f = 1.5$ m) in argon at the pressure of 60 kPa. (c) On-axis temporal evolution of the same pulse in the (t,z) plane.

In order to reproduce the experimental pulse shortening we choose parameters leading to an optimal compression in argon, i.e., $E_{\mathrm{in}} = 4$ mJ, $t_{\mathrm{FWHM}} = 45$ fs, $w_{\mathrm{FWHM}} = 11$ mm, and $f = 1.5$ m. This corresponds to an input peak power $P_{\mathrm{in}} = 5P_{\mathrm{cr}}$, where $P_{\mathrm{cr}} \simeq \lambda_0^2/2\pi n_0 n_2$ denotes the usual critical power for self-focusing of Gaussian beams. Figure 5 shows the peak intensity (solid curve), the beam diameter (FWHM of the fluence distribution, dashed curve) [Fig. 5(a)], the energy loss (solid curve) and peak electron density (dashed curve) [Fig. 5(b)] along the second half of the 2 m long propagation, which actually corresponds to the gas tube of the experimental setup. The nonlinear focus, from which the filament starts, arises at $z_c \simeq 1.45$ m, i.e., slightly before the linear focus of 1.5 m, in agreement with Marburger's formula [43]. The filament intensity reaches ~ 100 TW/cm^2 before relaxing to ~ 30 TW/cm^2 just after the linear focus.

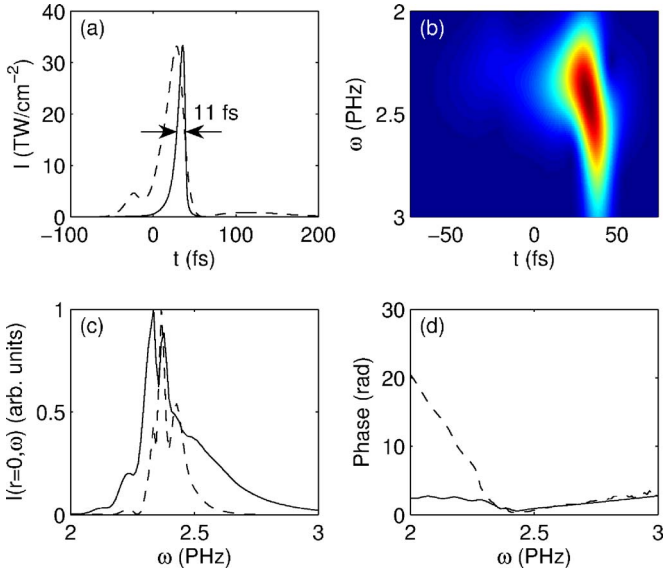

FIG. 6. (Color online) (a) On-axis intensity profiles vs time at $z=1.6$ m (dashed curve) and $z=2$ m (solid curve) for the same pulse as in Fig. 5. (b) XFROG trace of the on-axis fields at $z=2$ m computed using an unchirped 10 fs (FWHM) Gaussian reference pulse. (c) On-axis spectral intensity at $z=1.6$ m (dashed curve), $z=2$ m (solid curve), and (d) corresponding on-axis spectral phases for the same pulses with group delay adjusted for optimal visibility.

This behavior makes the electron density decrease from $\sim 10^{17}$ cm^{-3} to a lower level of $\sim 10^{13}$ cm^{-3}, along which the filament keeps a constant diameter of ~ 300 μm. This sudden intensity drop limits the ionization induced losses, which amount to only about 10% of the input pulse energy.

Figures 5(c) and 6(a) detail the on-axis ($r=0$) temporal evolution of the pulse in the (t,z) plane. First, at the nonlinear focus z_c, the front of the pulse focuses, and plasma depletes the rear part of the pulse. Second, at the position of the linear focus $z \simeq 1.5$ m the plasma density decreases, and the back of the pulse rises. Finally, from $z \simeq 1.6$ m, only the components close to center with intensity levels above 10^{13} W/cm^2 are effectively trapped in the filament, whereas the temporal wings diffract rapidly. This remarkable dynamics allow the formation of a temporally compressed "light bullet" of 11 fs duration in the core region of the filament: Both front and back of the initial pulse undergo collapse dynamics in the focal area and spread afterwards, whereas the pulse-center forms a narrow "waveguide" preserving its energy at low plasma density levels after the linear focus.

Figure 6(c) shows the corresponding on-axis intensity spectra, indicating strong spectral broadening mainly induced by self-phase modulation. For the most part this spectral broadening is restricted to the self-guided regime between $z \simeq 1.6$ m and $z \simeq 2$ m, and corresponds to temporal compression from 26 fs to 11 fs (FWHM) [see Fig. 6(a)]. Figure 2(d) represents the spectral phase at the same longitudinal distances. This spectral phase is numerically calculated from the Fourier transform of the complex field envelope and adjusted by subtracting a group delay corresponding to the shift of this envelope along the time direction as done with experimental data. Inside the self-guided regime between 1.6 and 2 m, the phase of the blue wing is almost flat, and we observe a characteristic kink when passing to the red wing. These features are in excellent agreement with our SPIDER measurements, displayed in Figs. 2(d) and 4(d). Moreover, we observe that the phase kink relaxes upon propagation in the "waveguide." This behavior must be attributed to the action of the operators T and T^{-1} in the propagation Eq. (1). We find it interesting to note in this context that we were not able to observe a similar pulse shortening for the above input pulse when setting these operators to unity.

IV. DISCUSSION

The comparison of Figs. 4 and 6 already revealed remarkable similarities between experimental data and numerical simulations. As the theoretical data display similar phase kinks as the measurements, we also computed XFROG traces from the former to achieve a better understanding of the spectrotemporal structure of the pulses. This spectrogram is shown in Fig. 6(b), and it displays a similar structure as the pulse shown in Fig. 4(b). The elongated leading tail is located in the red wing of the spectrum, i.e., as in the measurements. The blue part of the pulse taken by itself appears to be almost pedestal free and symmetric in time. As one can already expect by comparing the spectral data in Figs. 4 and 6, the red pedestal is less pronounced in the simulation data. We attribute this difference to initial perturbations in the experimental pulse shape, which was assumed to be Gaussian in the simulations. Comparing XFROG traces from different experimental shots reveal certain fluctuations in the extent and strength of this pedestal, whereas the compressible blue section remains relatively stable. This observation further supports this assumption.

When using filamentation for pulse compression, the spatiotemporal structure of the compressed pulse is an immediate concern. In particular, situations may arise where compression is limited to a small radial section in the pulse, which may render this method rather useless for practical applications. As a check on this, we computed in Fig. 7(a)–7(c) the power distribution inside circular regions of different diameters surrounding the filament. The solid curves correspond to the "compressor" exit at $z=2$ m, the dashed ones to $z=1.6$ m at the onset of "waveguide" formation. Actually only the central beam component with diameter $\varnothing = 100$ μm exhibiting the highest intensity supports self-compression to a duration of 11 fs [see Fig. 7(c)]. This is due to the fact that the front and rear part of the pulse are diffracted, whereas the pulse center is spatially focused, as is clearly visible in Fig. 7(d). Speaking in terms of energies, about 16% of the output energy are compressed to 28 fs [Fig. 7(a)], 6% to 15 fs [Fig. 7(b)] and about 1% of the output energy are compressed to 11 fs [Fig. 7(c)]. In this context, it is interesting to note that this shortening mechanism takes place in the post-ionization stage of the self-guiding range. Similar stable, long-living compressed temporal structures were numerically reported in the post-ionization dynamics of atmospheric femtosecond filaments [44].

So far, we have cleared up the mechanism underlying the observed pulse shortening. Also termed pulse compression,

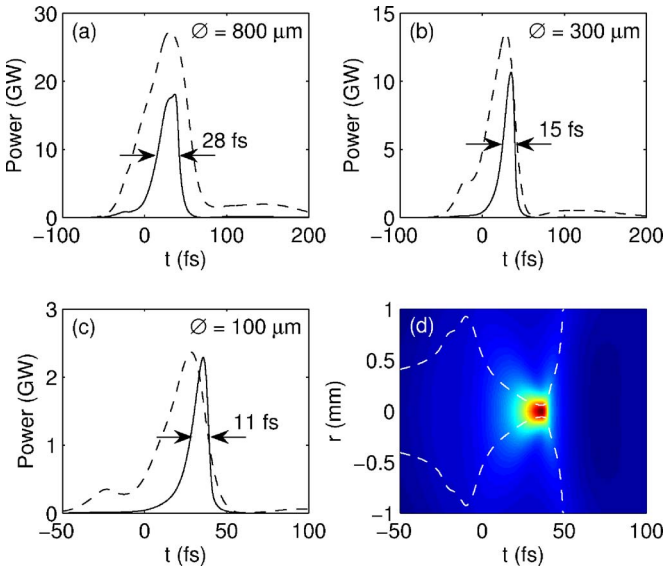

FIG. 7. (Color online) (a)–(c) Beam power vs time computed within a transverse zone with diameter ∅ for the same pulse as in Fig. 5 at $z=2$ m (solid curves) and $z=1.6$ m (dashed curves). (d) Intensity distribution at $z=2$ m. The white dashed lines mark the FWHM of the intensity vs time, where we computed the FWHM for each time slice according to its maximum.

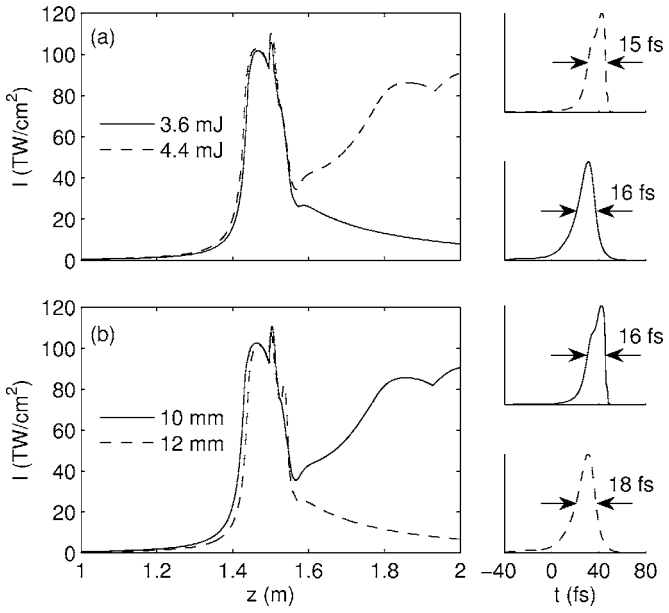

FIG. 8. Peak intensities of 45 fs (FWHM) focused ($f=1.5$ m) Gaussian pulses in Ar at the pressure of 60 kPa with (a) $P_{in}=4.5P_{cr}$ (solid curve) and $P_{in}=5.5P_{cr}$ (dashed curve) and 11 mm (FWHM) initial waist; (b) 10 mm (solid curve) and 12 mm (dashed curve) initial waist and $P_{in}=5P_{cr}$. Insets display the corresponding on-axis temporal profiles at the "compressor" exit at $z=2$ m.

this phenomenon resembles more a spatiotemporal redistribution resulting in the formation of a temporally short structure in the beam center only. In terms of power, we clearly have a trade off between compressed power and compression rate [Figs. 7(a)–7(c)].

Only the central high intensity component of the pulse is compressed (Fig. 7). For applications involving multiphoton processes, such as, e.g., high-harmonic generation, only this component will play a role. In order to estimate the diameter $\varnothing_N$ of the active section of the beam for an N-photon process we may use

$$\varnothing_N \simeq 2\sqrt{\frac{\int r^2 I^N r dr dt}{\int I^N r dr dt}}. \tag{6}$$

Computed from the intensity distribution of Fig. 7(d) we find $\varnothing_2 \simeq 820$ μm, but for $N=5$ we already have $\varnothing_5 \simeq 110$ μm.

Our experimental results show that the efficiency of pulse shortening crucially depends on the input beam parameters. In order to quantify these effects we performed several simulations summarized in Fig. 8. By varying either pulse energy or beam waist by ≈10% the observed pulse length at $z=2$ m is increased by more than 50%. Figure 8(a) shows the peak intensities of pulses having the same characteristics as before, except that their input power is either 4.5 (solid curve) or 5.5 times critical (dashed curve), which corresponds to 3.6 or 4.4 mJ, respectively. These pulses either diffract or relaunch another focusing and defocusing sequence, so that the durations attained in their most intense component at the exit ($z=2$ m) are larger than for the optimal configuration with 4 mJ (see insets). Figure 8(b) illustrates the same quantities at constant power ($5P_{cr}$), but with the FWHM beam waist varied from 10 mm (solid curve) to 12 mm (dashed curve). Modifying the beam waist essentially reproduces the behavior seen for variation of the input energy, with a higher energy being equivalent to a reduction of beam diameter. In particular, a second focusing and defocusing cycle is triggered for a narrower beam, while diffraction occurs more rapidly for a broader waist, yielding longer durations (see insets). Hence, for the present setup only the narrow interval of parameters centered around $w_{FWHM}=10$ mm and powers close to 5 times critical permits reaching pulse durations ~10 fs, i.e., less than one-quarter of the initial FWHM duration.

As the excitation of a new focusing sequence depends on the location of the nonlinear focus, z_c, the role of the focal length f also appears to be important and leads to analogous variations in the filament evolution (not shown here). By varying numerically the original focal length $f=1.5$ m by 10% and keeping all the other parameters unchanged, we observe an output FWHM duration of 14 fs for $f=135$ cm. In contrast, enlarging the focal length to $f=165$ cm gives about 11 fs duration at $z=2$ m, but the diminished beam divergence after the focal spot leads to a new focusing sequence, making the temporal output profile unstable upon propagation.

To complete the present analysis, we analyze the scalability of this pulse compression mechanism with respect to pulse energy and gas pressure. It must be pointed out that scalability is analyzed for a single femtosecond filament only. Due to our numerical scheme we do not take multiple filamentation into account, as observed in our experiments

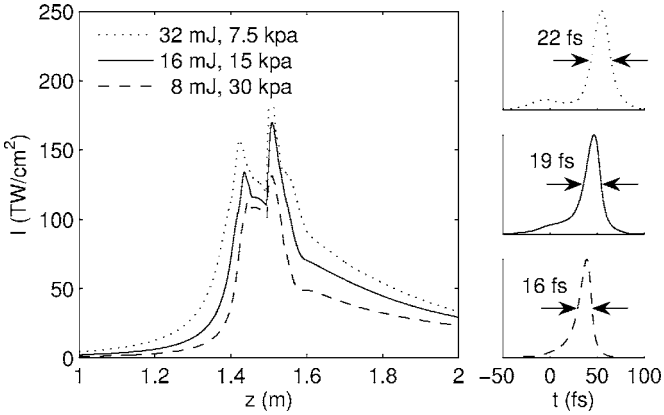

FIG. 9. Peak intensities of 45 fs (FWHM) focused ($f=1.5$ m) Gaussian pulses with $P_{in}=5P_{cr}$ and 11 mm (FWHM) initial waist propagating in Ar at the pressure of 30 kPa (dashed curve), 15 kPa (solid curve), and 7.5 kPa (dotted curve). Insets display the corresponding on-axis temporal profiles at the compressor exit at $z=2$ m.

for pulse energies larger than 5 mJ. Let us mention that at further elevated pulse energies the pulse breakup may be avoided, e.g., by suitable control of the spatial beam shaping. If we keep all other parameters as in Fig. 5, increase the pulse energy by a given scaling factor, and decrease the gas pressure by the same factor, then the ratio of the input power to the critical power will remain constant. Since the dynamics of the self-focusing due to the optical Kerr effect is dictated by this ratio, we can naively expect that the pulse compression works equally well. In certain limits these expectations are true, as revealed by Fig. 9. Even for a scaling factor of 8, the pulse duration is compressed by a factor of 2 compared to the initial 45 fs (dotted curve in Fig. 9). At this pulse energy and gas pressure we reach the limit of the validity of our model, since the peak electron density ($\rho \sim 5\times 10^{17}$ cm^{-3}) approaches the neutral atom density to within one order of magnitude.

Pulse compression seems to be less effective with increasing pulse energy and decreasing pressure. We explain this observation as follows: the maximum intensity is reached in the focal area. Its value, however, is determined by plasma defocusing and remains almost unchanged, whereas the input intensity is increased drastically. Hence, a larger part of the energy remains outside the center of the beam and spatial spreading of pulse front and back are less effective. For comparison, nonlinear losses were observed to increase to more than 15% for 32 mJ pulse energy.

Another limiting factor for compressing high-energy pulses is the onset of multiple filamentation, as observed in our experiments (see Sec. II). In the simulations, however, spatial multiple filamentation is *a priori* impossible due to the assumed rotational symmetry in transverse direction. Our model equations (1) and (2) are capable to describe the spatiotemporal dynamics of a single filament only. It is known that femtosecond filaments are azimuthally unstable [45]. These instabilities can lead to multiple filamentation, depending on filamentation length and initial perturbations of the beam profile.

V. CONCLUSION

The combination of experimental and theoretical methods sheds new light on the temporal dynamics inside a femtosecond filament. In this picture, an about fivefold compression of $\approx$50 fs appears sensible, when parameters are carefully adjusted to right below the onset of two fragmentation processes, a spatial and a spectrotemporal one. For delaying the spatial fragmentation, the high beam quality and high pulse-to-pulse stability of the kHz laser used for most of our studies appear to be of paramount importance, in particular when comparing with the studies done at 10 Hz. In contrast, it seems more difficult to completely avoid the spectrotemporal fragmentation, which leads to formation of a pulse pair rather than an isolated pulse. Our theoretical investigations clearly identify the initial beam collapse and subsequent refocusing events as the origin of this pulse splitting process. However, our studies also indicate a possibility to avoid the most detrimental implications of the temporal fragmentation as compression exclusively takes place in the newly generated blue part of the spectrum. In contrast, the red pedestal pulse exhibits several sharp spectral features, which correspond to elongated temporal structures, and is therefore poorly compressible. The dynamics in the blue wing of the spectrum appears to be much simpler, leading to a smooth spectral structure. The resulting blue subpulse is shaped upon propagation within the filament and reaches its shortest duration after several decimeters of propagation.

For a certain choice of experimental parameters, the two subpulses can be separated in time and also in frequency, such that simple (dispersionless) filtering may serve for a complete suppression of the pedestal in this scenario. Relative timing and weights of the two components appear highly dependent on the experimental parameters. Still, compressible pulse structures with a tolerable energy content of an incompressible pedestal can be found for input pulse energies ranging from about 2 to about 5 mJ. Our investigations indicate that both the onset of multiple filamentation as well as an increasing ionization degree of the plasma set a limit to scaling of filament self-compression towards much higher pulse energies. Similarly, as self-compression was not observed in the numerous experiments carried out below 1 mJ, this process seems possible only in a rather small window of pulse energies. Further studies need to show whether, for example, pressure gradients can be utilized to enlarge this parameter window to either side. Finally, the spatiotemporal structure of our pulse with increasing pulse duration at increasing beam radius may be of limited usefulness for low-order nonlinear processes, e.g., for pump-probe studies on a second-order nonlinearity. Yet, this structure does not play a role for the main application of such powerful few-cycle pulses. Even given the current constraints in input energy, our scheme appears to be extremely useful for experiments in extreme nonlinear optics, enabling experiments in attosecond physics, high-harmonic generation, and multiphoton ionization studies with unprecedented pulse energies and, simultaneously, a sub-10-fs temporal signature of the excitation pulse.

ACKNOWLEDGMENTS

The authors would like to thank Dr. R. Nuter and Dr. E. Cormier for their contribution concerning the photoionization of argon. Numerical simulations were performed on the machines of the CCRT at CEA-France and on the IBM p690 cluster (JUMP) of the Forschungs-Zentrum in Jülich, Germany. T. Sokollik and M. Schnürer acknowledge partial support by DFG Transregio TR18.

[1] C. V. Shank, R. L. Fork, R. Yen, R. H. Stolen, and W. J. Tomlinson, Appl. Phys. Lett. **40**, 761 (1982).
[2] G. Steinmeyer, D. H. Sutter, L. Gallmann, N. Matuschek, and U. Keller, Science **286**, 1507 (1999).
[3] V. E. Zakharov and A. B. Shabat, Sov. Phys. JETP **34**, 62 (1972).
[4] A. Hasegawa and F. Tappert, Appl. Phys. Lett. **23**, 142 (1973).
[5] F. M. Mitschke and L. F. Mollenauer, Opt. Lett. **12**, 407 (1987).
[6] G. I. Stegeman and M. Segev, Science **286**, 1518 (1999).
[7] A. Braun, G. Korn, X. Liu, D. Du, J. Squier, and G. Mourou, Opt. Lett. **20**, 73 (1995).
[8] Y. Silberberg, Opt. Lett. **15**, 1282 (1990).
[9] A. L. Gaeta, Phys. Rev. Lett. **84**, 3582 (2000).
[10] L. Bergé and A. Couairon, Phys. Rev. Lett. **86**, 1003 (2001).
[11] S. Champeaux and L. Bergé, Phys. Rev. E **68**, 066603 (2003).
[12] A. Couairon, M. Franco, A. Mysyrowicz, J. Biegert, and U. Keller, Opt. Lett. **30**, 2657 (2005).
[13] A. Couairon, J. Biegert, C. P. Hauri, W. Kornelis, F. W. Helbing, U. Keller, and A. Mysyrowicz, J. Mod. Opt. **53**, 75 (2006).
[14] H. R. Lange, J. F. Ripoche, A. A. Chiron, B. Lamouroux, M. A. Franco, B. Prade, E. T. J. Nibbering, and A. Mysyrowicz, in *Time-Space Self-Compression of Femtosecond Laser Pulses in Air*, OSA Technical Digest Series No. 7 (OSA, Washington D.C., 1998), p. 243.
[15] N. L. Wagner, E. A. Gibson, T. Popmintchev, I. P. Christov, M. M. Murnane, and H. C. Kapteyn, Phys. Rev. Lett. **93**, 173902 (2004).
[16] G. Stibenz, N. Zhavoronkov, and G. Steinmeyer, Opt. Lett. **31**, 274 (2006).
[17] M. Mlejnek, E. M. Wright, and J. V. Moloney, Opt. Lett. **23**, 382 (1998).
[18] M. Mlejnek, E. M. Wright, and J. V. Moloney, Phys. Rev. E **58**, 4903 (1998).
[19] C. P. Hauri, W. Kornelis, F. W. Helbing, A. Heinrich, A. Couairon, A. Mysyrowicz, J. Biegert, and U. Keller, Appl. Phys. B: Lasers Opt. **79**, 673 (2004).
[20] S. Henz and J. Herrmann, Phys. Rev. A **59**, 2528 (1999).
[21] H. Ward and L. Bergé, Phys. Rev. Lett. **90**, 053901 (2003).
[22] X. Chen, Y. Leng, J. Liu, Y. Zhu, R. Li, and Z. Xu, Opt. Commun. **259**, 331 (2006).
[23] A. Suda, M. Hatayama, K. Nagasaka, and K. Midorikawa, Appl. Phys. Lett. **86**, 111116 (2005).
[24] N. Zhavoronkov, Y. Gritsai, G. Korn, and T. Elsaesser, Appl. Phys. B: Lasers Opt. **79**, 663 (2004).
[25] C. Iaconis and I. A. Walmsley, IEEE J. Quantum Electron. **35**, 501 (1999).
[26] G. Stibenz and G. Steinmeyer, Opt. Express **12**, 6319 (2004).
[27] G. Stibenz and G. Steinmeyer, Rev. Sci. Instrum. **77**, 073105 (2006).
[28] D. Keusters, H. S. Tan, P. O'Shea, E. Zeek, R. Trebino, and W. S. Warren, J. Opt. Soc. Am. B **20**, 2226 (2003).
[29] S. Linden, H. Giessen, and J. Kuhl, Phys. Status Solidi B **206**, 119 (1998).
[30] J. M. Dudley, X. Gu, L. Xu, M. Kimmel, E. Zeek, P. O'Shea, R. Trebino, S. Coen, and R. S. Windeler, Opt. Express **10**, 1215 (2002).
[31] R. Wiehle, B. Witzel, H. Helm, and E. Cormier, Phys. Rev. A **67**, 063405 (2003).
[32] E. Cormier, P. A. Hervieux, R. Wiehle, B. Witzel, and H. Helm, Eur. Phys. J. D **26**, 83 (2003).
[33] S. Skupin and L. Bergé, Physica D **220**, 14 (2006).
[34] A. Dalgarno and A. E. Kingston, Proc. R. Soc. London, Ser. A **259**, 424 (1960).
[35] Y. Shimoji, A. T. Fay, R. S. F. Chang, and N. Djeu, J. Opt. Soc. Am. B **6**, 1994 (1989).
[36] P. Sitz and R. Yaris, J. Chem. Phys. **49**, 3546 (1968).
[37] V. Mizrahi and D. P. Shelton, Phys. Rev. Lett. **55**, 696 (1985).
[38] M. Nisoli, S. D. Silvestri, and O. Svelto, Appl. Phys. B: Lasers Opt. **68**, 2793 (1996).
[39] H. J. Lehmeier, W. Leupacher, and A. Penzkofer, Opt. Commun. **56**, 67 (1985).
[40] P. B. Corkum and C. Rolland, "Self-focusing and continuum generation in gases," in *The Supercontinuum Laser Source*, edited by R. R. Alfano (Springer-Verlag, Germany, 1989), Chap. 7, p. 318.
[41] A. M. Perelomov, V. S. Popov, and M. V. Terent'ev, Sov. Phys. JETP **23**, 924 (1966).
[42] T. Brabec and F. Krausz, Phys. Rev. Lett. **78**, 3282 (1997).
[43] J. H. Marburger, Prog. Quantum Electron. **4**, 35 (1975).
[44] S. Champeaux and L. Bergé, Phys. Rev. E **71**, 046604 (2005).
[45] S. Skupin, U. Peschel, C. Etrich, L. Leine, D. Michaelis, and F. Lederer, Opt. Lett. **27**, 1812 (2002).